

SQUID-Detected Magnetic Resonance Imaging in Microtesla Magnetic Fields

R. McDermott^{1,2,*}, N. Kelso^{1,2}, S-K. Lee^{1,2}, M. Mölle^{1,2},
M. Mück^{1,2,†}, W. Myers^{1,2}, B. ten Haken^{1,2,‡}, H.C. Seton⁴,
A.H. Trabesinger^{1,3,§}, A. Pines^{1,3}, and J. Clarke^{1,2}

¹Materials Sciences Division, Lawrence Berkeley National Laboratory,
Berkeley, CA 94720, USA

Departments of ²Physics and ³Chemistry, University of California,
Berkeley, CA 94720, USA

⁴Department of Bio-Medical Physics and Bio-Engineering, University of Aberdeen,
Aberdeen AB9 2TD, UK

We describe studies of nuclear magnetic resonance (NMR) spectroscopy and magnetic resonance imaging (MRI) of liquid samples at room temperature in microtesla magnetic fields. The nuclear spins are prepolarized in a strong transient field. The magnetic signals generated by the precessing spins, which range in frequency from tens of Hz to several kHz, are detected by a low-transition temperature dc SQUID (Superconducting QUantum Interference Device) coupled to an untuned, superconducting flux transformer configured as an axial gradiometer. The combination of prepolarization and frequency-independent detector sensitivity results in a high signal-to-noise ratio and high spectral resolution (~ 1 Hz) even in grossly inhomogeneous magnetic fields. In the NMR experiments, the high spectral resolution enables us to detect the 10-Hz splitting of the spectrum of protons due to their scalar coupling to a ^{31}P nucleus. Furthermore, the broadband detection scheme combined with a non-resonant field-reversal spin echo allows the simultaneous observation of signals from protons and ^{31}P nuclei, even though their NMR

*Current address: National Institute of Standards and Technology, Boulder, Colorado 80305, USA

†Current address: Institute of Applied Physics, Justus Liebig University, 35392 Giessen, Germany

‡Current address: University of Twente, Low Temperature Division, 7500 AE Enschede, The Netherlands

§Current address: ETH Zürich, Laboratory of Physical Chemistry, CH-8093 Zürich, CH-8092 Zürich, Switzerland

resonance frequencies differ by a factor of 2.5. We extend our methodology to MRI in microtesla fields, where the high spectral resolution translates into high spatial resolution. We demonstrate two-dimensional images of a mineral oil phantom and slices of peppers, with a spatial resolution of about 1 mm. We also image an intact pepper using slice selection, again with 1-mm resolution. In further experiments we demonstrate T_1 -contrast imaging of a water phantom, some parts of which were doped with a paramagnetic salt to reduce the longitudinal relaxation time T_1 . Possible applications of this MRI technique include screening for tumors and integration with existing multichannel SQUID systems for brain imaging.

KEY WORDS: SQUID; nuclear magnetic resonance; magnetic resonance imaging.

1. INTRODUCTION

Nuclear magnetic resonance (NMR)^{1,2} is one of the most powerful tools to emerge from fundamental physics. It is widely used to investigate molecular structure and conformation at magnetic fields that range up to 21 T, corresponding to a resonance frequency of around 900 MHz for the proton. Because the NMR frequency is a direct measure of the local magnetic field experienced by a given nucleus, NMR spectroscopy is an extremely sensitive probe of the interactions of the nucleus with its electromagnetic environment. In magnetic resonance imaging (MRI)³⁻⁵, the application of magnetic field gradients enables one to image the human body noninvasively with extraordinary clarity, typically in a field of 1.5 T at a frequency of about 64 MHz. However, despite the tremendous successes of high-field NMR spectroscopy and MRI, there has long been interest in performing NMR and MRI in much lower magnetic fields.⁶⁻⁹ The NMR signal in many low-field experiments has been detected with a dc Superconducting QUantum Interference Device (SQUID) which is an exquisitely sensitive detector of magnetic field when coupled to a suitable input circuit.¹⁰ In his review, Greenberg¹¹ lists some 100 different SQUID-based experiments on gases, liquids and solids at nuclear temperatures that range from 300 K down to below 1 μ K.

Recently, it was demonstrated that one could obtain high resolution NMR spectra (linewidths ~ 1 Hz) from liquids at frequencies as low as 100 Hz in grossly inhomogeneous magnetic fields.¹² This approach combines the benefits of prepolarization of the nuclear spins with untuned SQUID detection, which provides a frequency-independent sensitivity. The technique was subsequently extended to MRI at frequencies of about 5 kHz, yielding images with a spatial resolution of about 1 mm.¹³ In an alternative, ear-

lier approach, Seton *et al.*¹⁴ obtained magnetic resonance images with good spatial resolution using a tuned SQUID receiver to detect the NMR signals from thermally polarized spins at a frequency of 425 kHz.

In this article, we describe the motivation, design, implementation and results of experiments on low-frequency NMR and MRI using prepolarization and untuned SQUID detection. In Sec. 2, we briefly review the principles of the SQUID and of NMR and MRI. Section 3 is concerned with NMR spectroscopy, and demonstrates the enhanced spectral resolution and increased signal-to-noise ratio (SNR) that can be achieved by lowering the magnetic field in which the data are acquired. Section 4 describes the MRI system, including details of the cryogenics, imaging coils and associated electronics, steps taken to reduce the system noise, and a selection of images. Conclusions and suggestions for future work are presented in Sec. 5.

This paper is dedicated to the memory of Olli Lounasmaa, a good friend to one of us (JC) for some 30 years. This research embraces two of his major interests. Olli did much to bring SQUIDS to Finland, and greatly encouraged their use in neuromagnetism. He was also deeply involved in the use of SQUIDS to study nuclear ordering in copper and silver at ultralow temperatures.

2. SQUIDS, NMR and MRI

2.1. The dc SQUID

The dc SQUID¹⁵ combines the macroscopic quantum phenomena of Josephson tunneling¹⁶ and flux quantization.¹⁷ In a Josephson junction, Cooper pairs tunnel coherently through the tunnel barrier, and constitute a supercurrent for applied currents up to a critical value I_0 ; for higher currents, a voltage is developed across the junction. Flux quantization refers to the fact that magnetic flux contained in a closed superconducting loop is quantized in units of the flux quantum, $\Phi_0 \equiv h/2e \approx 2.07 \cdot 10^{-15}$ Tm². The SQUID consists of two Josephson junctions connected in parallel on a superconducting loop, as shown schematically in Fig. 1. Each junction has a self-capacitance C and is shunted with a thin-film resistor (not shown). The value of this resistor, R , is chosen to satisfy the constraint^{18,19} $\beta_c \equiv 2\pi I_0 R^2 C / \Phi_0 \leq 1$, which ensures the current-voltage characteristic is nonhysteretic. The bias current $I_b > 2I_0$ flowing through the two junctions produces a voltage V across the device. When the magnetic flux Φ threading the loop is changed, the voltage across the SQUID oscillates with a period Φ_0 , with maxima at $(2n+1)\Phi_0/2$ and minima at $n\Phi_0$, where n is an integer. One generally operates the SQUID with a flux bias near $(2n+1)\Phi_0/4$, where

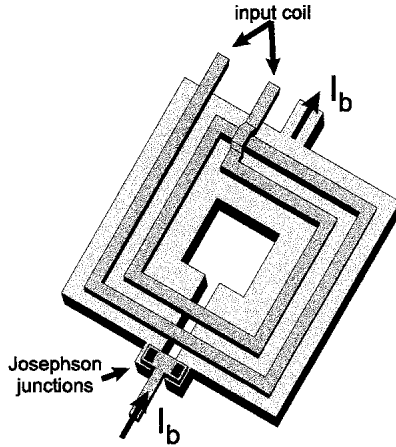


Fig. 1. Square washer SQUID, with integrated superconducting input coil. The two Josephson junctions are biased with a current I_b .

the transfer function $|\partial V/\partial \Phi|$ is a maximum. A small change in flux ($\ll \Phi_0$) gives rise to a change in voltage that is detected with an amplifier.

Most SQUIDs used today are based on the square washer design,²⁰ shown in Fig. 1, and grown on silicon wafers. The washer is patterned in a thin film of Nb, and the junctions are fabricated from a Nb-AlO_x-Nb trilayer.²¹ Magnetic flux is coupled to the SQUID by means of a current applied to the integrated Nb coil, which is electrically insulated from the washer. Optimum performance is achieved when the SQUID inductance L satisfies the constraint²² $\beta_L \equiv 2LI_0/\Phi_0 \approx 1$. It is necessary to choose the parameters so that $2\pi k_B T/I_0 \Phi_0 \ll 1$ and $2\pi k_B T \ll \Phi_0^2/2L$ to make the effects of thermal fluctuations negligible. For a typical SQUID used at 4.2 K, a representative set of parameters is $L = 100$ pH, $I_0 = 10$ μ A, $C = 0.5$ pF and $R = 6$ Ω . The predicted value of $|\partial V/\partial \Phi| \approx R/L$ is approximately 100 μ V/ Φ_0 , and the predicted flux noise $(16k_B T L^2/R)^{1/2} \approx 1$ $\mu\Phi_0$ Hz^{-1/2}. For low-frequency applications, the SQUID is almost invariably operated in a flux-locked loop that maintains the flux threading it at a constant value. The flux-locked loop enables one to track changes in flux corresponding to many flux quanta, and produces an output voltage proportional to the applied flux. One can make a magnetometer by connecting a superconducting loop to the input coil to form a closed superconducting circuit; in the absence of external noise, a typical noise level is ~ 1 fT Hz^{-1/2}. The response of the SQUID to an applied magnetic flux is independent of frequency until the flux-locked loop begins to roll off at frequencies that range typically from 50 kHz to several megahertz.

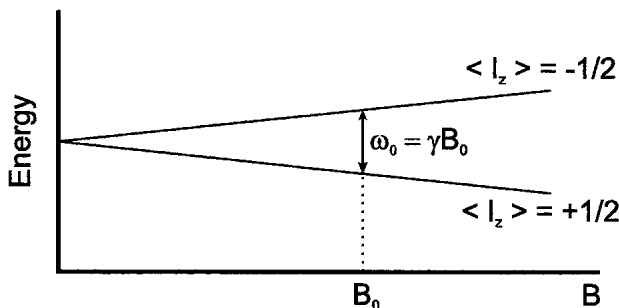


Fig. 2. Energy level diagram for a spin- $\frac{1}{2}$ nucleus in a magnetic field B .

2.2. Elements of NMR

The essence of NMR is the interaction of the magnetic moment of a nuclear spin with an externally applied magnetic field.^{1,2} For simplicity, we consider the case of a single spin- $\frac{1}{2}$ nucleus subjected to a uniform magnetic field $\mathbf{B} = B_0 \hat{\mathbf{k}}$ along the z -direction (Fig. 2). The Hamiltonian is

$$H = \gamma \hbar B_0 I_z \quad (1)$$

where \mathbf{I} is the spin angular momentum operator of the nucleus, and γ is its magnetogyric ratio; for the proton, $\gamma = 2.67 \cdot 10^8 \text{ rad T}^{-1}\text{s}^{-1}$. The eigenstates $|+\rangle$ and $|-\rangle$ correspond to the nuclear spin being aligned parallel and antiparallel to the magnetic field, respectively: $\langle I_z \rangle = +\frac{1}{2}$ and $\langle I_z \rangle = -\frac{1}{2}$. Here, I_z is the projection of I on the z -axis. The energy eigenvalues are

$$E = \pm \frac{1}{2} \gamma \hbar B_0, \quad (2)$$

and the angular frequency corresponding to a transition between levels—known as the Larmor frequency—is

$$\omega_0 = \gamma B_0 \quad (3)$$

To observe the resonance phenomenon, one applies an oscillatory magnetic field

$$\mathbf{B}_1(t) = B_1(\hat{\mathbf{i}} \cos \omega t + \hat{\mathbf{j}} \sin \omega t) \quad (4)$$

in the x - y plane at a frequency ω which is close to the Larmor frequency. The excitation field \mathbf{B}_1 tips the nuclear spins away from the z -direction, with a tip angle that is determined by the amplitude and duration of the excitation field. In the simplest pulsed NMR experiment (Fig. 3a), the excitation field \mathbf{B}_1 is chosen such that its amplitude and duration τ satisfy the condition

$$\gamma B_1 \tau = \pi/2. \quad (5)$$

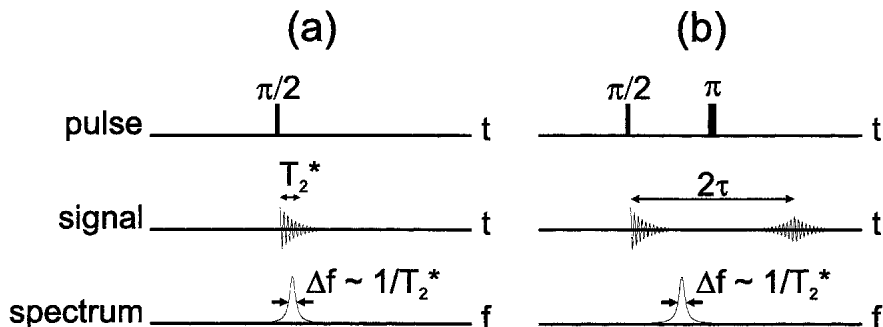


Fig. 3. Essence of the pulsed NMR experiment. (a) A resonant $\pi/2$ pulse tips the sample magnetization into the transverse plane. Precession of the nuclear spins in the transverse plane produces a free induction decay (FID) with a decay time T_2^* . Fourier transform of the FID yields the NMR spectrum with linewidth Δf . (b) Spin-echo sequence.

In this case, the excitation rotates the magnetization away from the direction of the static field into the transverse plane. Following the application of the $\pi/2$ pulse, the spins evolve under the influence of the Hamiltonian [Eq. (1)]; the resulting precession or free induction decay (FID) is detected, conventionally by coupling the flux into an inductor in parallel with a capacitor to form a resonant circuit tuned to the NMR frequency. The Fourier transform of the FID yields the NMR spectrum.

There are two important times which govern nuclear relaxation in an NMR experiment. The spin-lattice or longitudinal relaxation time T_1 determines the characteristic timescale for spins to align with an external magnetic field; this process involves spin-flips, and therefore exchange of energy with a thermal reservoir (in a solid, the lattice). The spin-spin or transverse relaxation time T_2 is the characteristic time following excitation over which spins lose phase coherence in the transverse plane. In a pulsed NMR experiment, in the absence of additional dephasing mechanisms that further broaden the line, T_2 determines the duration of the FID.

Generally, however, variation of the strength of the B_0 field over the volume of the sample yields a distribution of Larmor frequencies in the spin ensemble; as the spins evolve at slightly different frequencies, they lose phase coherence, leading to a decay of signal amplitude (in the time domain) and a broadening of the NMR line (in the frequency domain). When the NMR linewidth is dominated by magnetic field inhomogeneity, one speaks of an effective spin-spin relaxation time $T_2^* < T_2$. For example, in a high-field spectrometer operating at 500 MHz, a homogeneity of 20 parts per billion

over the sample volume leads to a dispersion of Larmor frequencies of roughly 10 Hz, corresponding to $T_2^* \sim 100$ ms. In this case, inhomogeneous broadening renders it impossible to resolve spectral features at the level of a few Hz; moreover, the line broadening leads to a degradation of the signal-to-noise ratio (SNR) in the frequency domain. We note, however, that phase coherence which is lost due to field inhomogeneity can be recovered using the technique of Hahn spin echoes.²³ The spin echo sequence (Fig. 3b) is written as $\pi/2-\tau-\pi-\tau$ -acquire, where $\pi/2$ and π specify the tip angles of the rf pulses, and τ refers to intervals of free precession of the nuclear spins. The effect of the π pulse is to invert the phase of all nuclei in the ensemble. As the spins evolve during the second interval τ , any spurious phase acquired during the first interval τ is "unwound", and at time 2τ the echo amplitude is a maximum.

In NMR spectroscopy, one is concerned with the fine structure of the NMR spectrum which is due to interaction of the nucleus with its local electromagnetic environment. For a sample in the liquid state, two types of interaction are important: chemical shift, and scalar coupling or J -coupling. These give rise to shifts and splittings, respectively, in the NMR lines. The chemical shift²⁴ arises from the diamagnetic screening of an applied magnetic field by the electron cloud which surrounds the nucleus, and therefore scales with the strength of the applied field. On the other hand, the J -coupling²⁵ is independent of the strength of the applied field. In the limit of weak coupling, the interaction Hamiltonian for spin- $\frac{1}{2}$ is written as

$$H_J = 2\pi\hbar J \mathbf{I}_{A_z} \mathbf{I}_{B_z}, \quad (6)$$

where \mathbf{I}_A and \mathbf{I}_B are the spins of the coupled nuclei, and the parameter J expresses the strength of the coupling. In general, scalar coupling to n magnetically equivalent nuclei A splits the resonance of nucleus B into $n+1$ equally spaced lines; the relative intensity of the i th line is determined from the binomial coefficient $\binom{n}{i-1}$. The scalar coupling strengths—the magnitude of the resonance splittings—act as signatures of specific chemical bonds.

Finally, we note that while the majority of NMR studies have been performed at high magnetic fields in the range from tesla to tens of tesla, considerations of cost and complexity of the experimental apparatus have long motivated investigations of nuclear magnetism at low magnetic field strengths, of the order of the Earth's field $\sim 50 \mu\text{T}$.⁹ The main obstacle to these studies is the intrinsically small signal produced by low fields. For thermally polarized nuclei, the sample magnetization scales linearly with the strength of the magnetic field. Since the Larmor frequency is also directly proportional to field strength, conventional Faraday law detection yields a quadratic dependence of the detected NMR signal amplitude on magnetic

field. However, prepolarization⁶ in a strong transient field can be used to create a nuclear magnetization which is independent of measurement field. Moreover, detection with an untuned SQUID magnetometer, which measures flux rather than rate of change of flux, can be used to remove the frequency- dependence of the NMR receiver. These elements are central to the microtesla field NMR and MRI experiments described below.

2.3. Elements of MRI

The idea of using NMR to acquire images of objects containing nuclear spins was proposed independently by Lauterbur³ and by Mansfield and Grannell⁴ in the early 1970s. The essential principle is as follows. When a sample containing NMR-active nuclei is subjected to both a homogeneous static magnetic field and known magnetic field gradients, the Larmor frequency of spins in the sample becomes a known function of their location. From the NMR spectrum, therefore, it is possible to extract information about the spatial distribution of nuclear spins in the sample.⁵ The simplest case is that of a one-dimensional projection (Fig. 4). The sample is placed in a uniform field oriented in the z -direction $\mathbf{B} = B_0 \hat{\mathbf{k}}$. In addition to the uniform field, one applies a constant magnetic field gradient $G_z \equiv dB_z/dz$. The local magnetic field at a point within the sample is thus given by

$$B(z) = B_0 + zG_z, \quad (7)$$

and the local Larmor frequency $\omega(z)$ becomes

$$\omega(z) = \gamma(B_0 + zG_z). \quad (8)$$

Since the strengths of the applied magnetic field and field gradient are known, it is possible to map directly from the Larmor frequency to a position along the z -axis. The NMR spectrum obtained from the sample yields a projection of nuclear spin density onto the z -axis.

The quadratic dependence of NMR signal strength on magnetic field has for decades fueled the drive to higher fields in MRI scanners. At the same time, there have been continued efforts toward the development of MRI systems which operate at low magnetic field strengths.⁷ Such systems are potentially less expensive and less demanding of infrastructure than existing high field scanners, which rely on superconducting magnets to generate extremely homogeneous, stable magnetic fields in the range 1–10 tesla. Moreover, despite the serious disadvantage of reduced sensitivity, the images acquired in low field should, in principle, be of higher quality than those acquired in high magnetic field. An inevitable drawback of high-field imaging

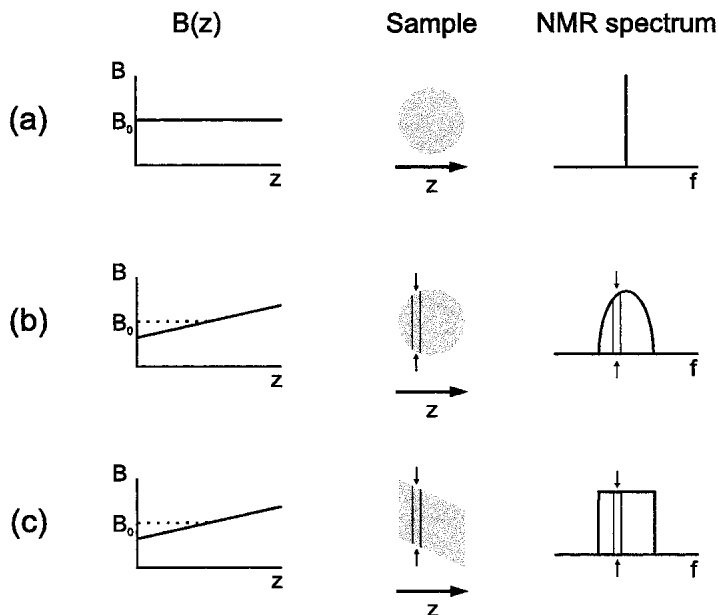


Fig. 4. One-dimensional MRI projection with frequency encoding. (a) Circular sample in a uniform field. (b) Circular sample in a magnetic field with constant field gradient G_z . (c) Trapezoidal sample in a magnetic field with constant field gradient G_z . Arrows show correspondence between real space and frequency space.

is that of susceptibility artifacts. When a heterogeneous sample is placed in a magnetic field, variations in magnetic susceptibility over the sample volume give rise to spurious magnetic field gradients. When these spurious gradients become comparable to the gradients which are used for encoding, the image is severely distorted. Since the strength of the spurious gradients scales linearly with the strength of the applied field, it is possible to eliminate susceptibility-induced distortions by imaging in low magnetic field.²⁶ Finally, T_1 -contrast is enhanced in low magnetic fields. In T_1 -contrast imaging, one either takes advantage of differences in T_1 in different tissue types, or introduces a paramagnetic contrast agent which selectively reduces T_1 at the sites where it is absorbed. To obtain T_1 -contrast images, one acquires MRIs with different repetition times. For long repetition times, nearly all regions of the sample have recovered to essentially full magnetization prior to the application of the next $\pi/2$ pulse; for short repetition times, however, the magnetization has recovered substantially only in those regions of the sample where T_1 is short, so that these regions are selectively highlighted in

the image. Because nuclear relaxation processes are more strongly dependent on the correlation time at low frequencies than at high frequencies,²⁷ low-field T_1 -contrast images allow sharper differentiation of tissues than the corresponding images acquired in high field. The enhanced T_1 -contrast in the Earth's field range has been demonstrated elegantly by Planinšič *et al.*²⁸

3. MICROTESLA FIELD NMR SPECTROSCOPY

Line broadening caused by inhomogeneities in the magnetic field is a major liability in liquid-state NMR. Spectral resolution and hence the information one can extract about the interaction of nuclei with the local electromagnetic environment is ultimately determined by the width of the NMR lines: it is necessary for the strength of the interactions to exceed the dispersion of Larmor frequencies in the sample. Moreover, for a fixed sample magnetization, the frequency domain SNR achieved from a single FID or spin echo signal scales inversely with the inhomogeneously broadened width of the NMR line. For these reasons, high-resolution liquid-state NMR or MRI typically requires exquisite field homogeneity. In conventional high-field systems, homogeneity is attained by supplementing the magnet with sophisticated and costly shim coils.

An appealing alternative is simply to reduce the strength of the measurement field. For a fixed *relative* field homogeneity, the *absolute* homogeneity is enhanced by decreasing the strength of the magnetic field. While the sensitivity of the conventional tuned circuit detector falls off rapidly as field strength is reduced, this is not the case for the untuned SQUID magnetometer, which is sensitive to magnetic flux, rather than the rate of change of magnetic flux. Consequently, for a fixed sample magnetization, the integrated intensity of the NMR signal—the area under the peak—is independent of frequency. It is therefore possible to perform the following unconventional NMR experiment.

The sample of nuclear spins is prepolarized in a magnetic field B_p , typically 1–100 mT, for a time much greater than T_1 . In addition, a much smaller measurement field B_0 is applied in an orthogonal direction. The polarizing field is then removed nonadiabatically, in a time much less than ω_0^{-1} , inducing spin precession about B_0 . In this experiment, the sample magnetization is fixed by the strength of the polarizing field, while the width of the NMR line is determined by the absolute homogeneity of the measurement field. Assuming the line is initially inhomogeneously broadened, as B_0 is reduced the NMR line is compressed into a narrower band and the peak height grows. Thus, both spectral resolution and SNR are enhanced.

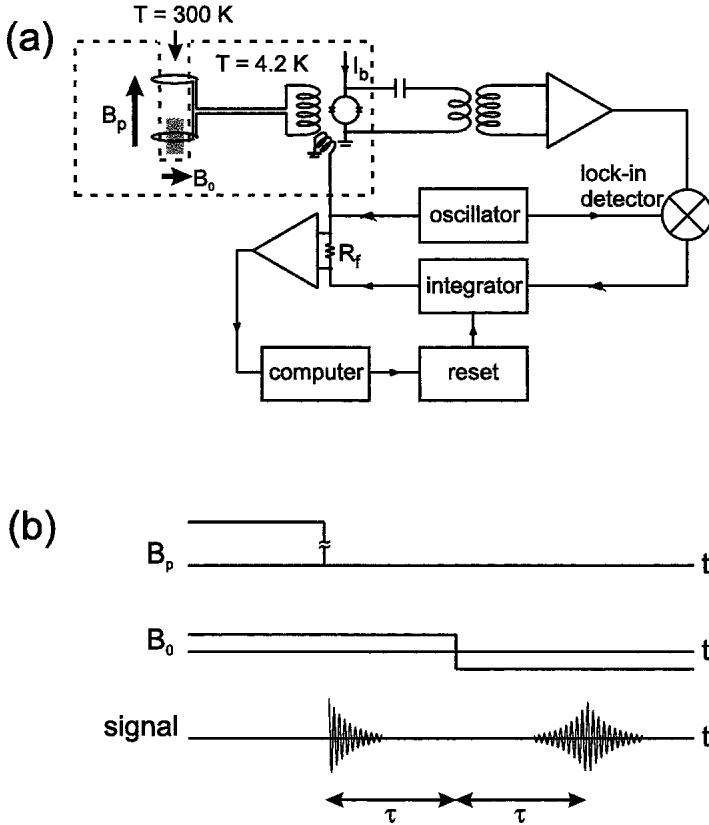


Fig. 5. (a) Experimental configuration for microtesla field NMR. Dashed lines enclose components at 4.2 K. (b) NMR pulse sequence involving nonadiabatic removal of the polarizing field B_p and spin echo obtained by reversal of the measurement field B_0 .

Figure 5a shows schematically an experiment designed to implement the concepts described above. The superconducting input coil of the SQUID was connected to a first- derivative gradiometer, wound from 75- μm Nb wire on a G-10 fiberglass tube, with loop diameters of 38 mm and a baseline of 80 mm. The tube was fitted onto the tail of a double-walled Pyrex insert which was immersed in liquid helium along with the SQUID and gradiometer. A Pyrex cell containing the liquid sample was lowered into the tail section of the insert to occupy the lower loop of the gradiometer; a heater maintained the sample at about 300 K. The gradiometer attenuated uniform external field noise by two orders of magnitude. The current-biased SQUID, surrounded

with a superconducting Pb shield, was flux modulated¹⁰ at 2 MHz with a peak-to-peak amplitude of $\Phi_0/2$. The resultant oscillating voltage across the SQUID was amplified by a room-temperature transformer and a low-noise preamplifier. After lock-in detection the signal was integrated and coupled via a resistor R_f into a second coil coupled to the SQUID to provide negative feedback. The signal voltage across R_f was amplified and stored in a computer.

The NMR pulse sequence is shown in Fig. 5b. The polarizing field B_p , of the order of 1 mT, was applied along the axis of the gradiometer by means of a current of the order of 1 A in a solenoid of Cu wire wound directly on the sample cell. An orthogonal measurement field B_0 of the order of microtesla was supplied by a Helmholtz pair in the helium bath. Nonadiabatic removal of the polarizing field induced spin precession in the much weaker measurement field. Subsequently, nonadiabatic reversal of the measurement field direction was used to reverse the sense of the spin precession, and thus to form a spin echo. During the polarizing interval, the flux-locked loop was disabled by shorting out the integrating capacitor; the loop was reset about 10 ms after the reversal of the measurement field. A superconducting weak link in series with the gradiometer coils prevented the coupling of large currents into the input coil of the SQUID.

Figure 6 demonstrates the SNR enhancement achieved by reducing the measurement field strength. We first acquired a spectrum from a sample of mineral oil (proton density ~ 100 Molar) in a static magnetic field of 1.8 mT using a conventional Hahn spin echo sequence. Figure 6a shows the proton resonance at 77 kHz, with a linewidth of about 1 kHz. The broad linewidth is a measure of the poor homogeneity of the static field, about 10,000 ppm. Figure 6b shows the NMR signal from the same volume of mineral oil, measured in a field of 1.8 μ T using the sequence of Fig. 5b. The sample was polarized in a field of about 2 mT, and the measurement field was generated by the same magnet used to acquire the spectrum in the upper panel. The proton resonance appears at 77 Hz, and the linewidth has been reduced to about 1 Hz. The sample magnetizations are the same in these two experiments; moreover, as the detector is untuned, the areas under the NMR lines are also the same. However, when the proton resonance was lowered from 77 kHz to 77 Hz, the NMR linewidth was compressed by a factor of 1000, and the peak height grew by the same factor. Reduction in the measurement field by a factor of 1000 therefore yielded an SNR enhancement of roughly 1000—note that Fig. 6a represents the average of 10,000 transients, while Fig. 6b was obtained by averaging only 100 transients. In measurement fields of around 1 μ T we typically achieved SNR of a few tens without signal averaging from samples with a volume of a few milliliters and a polarization

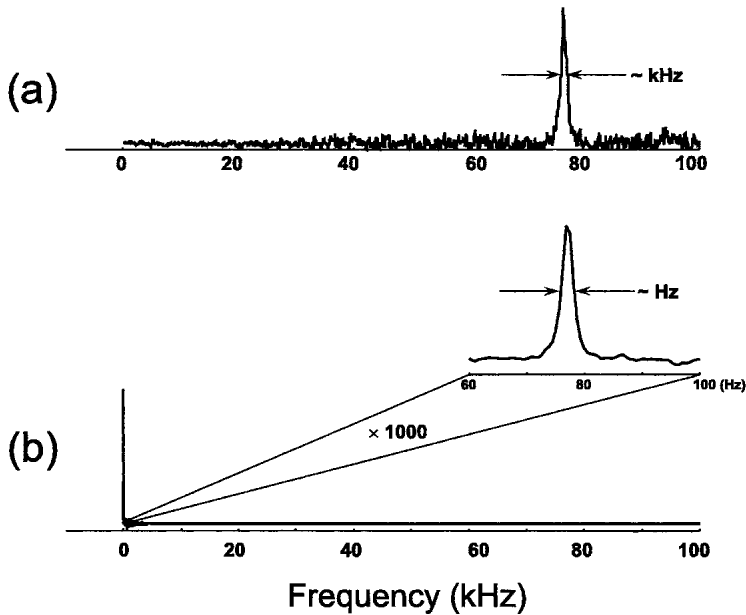


Fig. 6. Linewidth narrowing and SNR enhancement of NMR spectrum of 5 mL of mineral oil through reduction of measurement field. (a) Spectrum acquired in static field of 1.8 mT using spin-echo sequence of Fig. 3b, averaged over 10,000 transients. (b) Spectrum acquired in field of 1.8 T using the sequence of Fig. 5b with $B_p = 1.8$ mT, averaged over 100 transients. Measurement field coil was the same as in (a).

of the order of 10^{-8} .

The high spectral resolution we have achieved with NMR detection in low field makes it possible to determine scalar coupling strengths accurately, even in inhomogeneous measurement fields. Figure 7a shows the NMR spectrum obtained from the ester trimethyl phosphate in a field of $4.6 \mu\text{T}$. Scalar coupling of the protons to the ^{31}P nucleus causes the proton resonance to split into a doublet, with a coupling strength $J_3[P, H] = 10.4 \pm 0.6$ Hz which is characteristic of this particular next-next-nearest neighbor interaction. The proton doublet is easily resolved in a field of $4.8 \mu\text{T}$, despite the very poor relative field homogeneity of about 10,000 ppm over the sample volume.

Finally, the broadband sensitivity of the untuned SQUID magnetometer, together with the broad range of excitation frequencies produced by the sequence of Fig. 5b, can be exploited for the simultaneous detection of resonances from nuclei with different magnetogyric ratios γ , resonating at different frequencies. As an example, Fig. 7b shows the NMR spectrum of

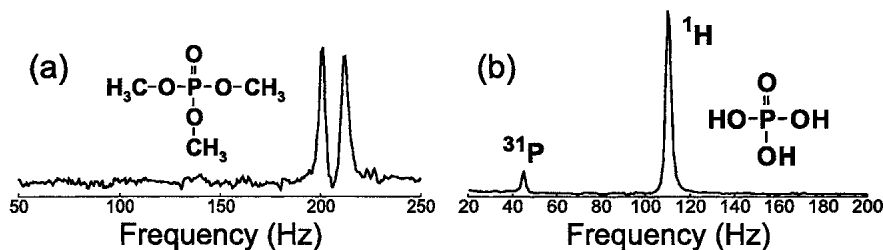


Fig. 7. Microtesla NMR spectra. (a) NMR spectrum of 3 mL of neat trimethyl phosphate (Sigma-Aldrich) measured in $4.8\ \mu\text{T}$, averaged over 100 transients. Electron-mediated scalar coupling of the nine equivalent protons to the ^{31}P nucleus splits the proton resonance into a doublet, with a splitting of $10.4 \pm 0.6\ \text{Hz}$. (b) NMR spectrum of 5 mL of 85% phosphoric acid (H_3PO_4) measured in $2.6\ \mu\text{T}$, averaged over 1000 transients. The magnetogyric ratios of the spin- $\frac{1}{2}$ nuclei ^{31}P and ^1H differ by a factor of 2.5, yielding resonances at 44 Hz and 110 Hz, respectively.

the protons and ^{31}P nuclei acquired from a sample of phosphoric acid in a field of $2.6\ \mu\text{T}$. The relative intensity of the two lines is determined by the different spin densities of the two nuclear species, and by the difference in magnetizations resulting from the different magnetogyric ratios.

4. MICROTESLA FIELD MRI

4.1. Concept and introduction

There is an intimate connection between the inhomogeneously broadened NMR linewidth and the spatial resolution achievable in MRI. We can understand this relationship by examining the simple case of frequency encoding in one dimension. We consider an MRI phantom consisting of two samples of nuclear spins, separated by some distance along the z -axis (Fig. 8). The phantom is placed in a nominally homogeneous magnetic field $\mathbf{B} = B_0\hat{\mathbf{k}}$. If, however, there are spurious magnetic field gradients (e.g. off-diagonal gradient components $G_x \equiv dB_z/dx$ and $G_y \equiv dB_z/dy$), the NMR line acquired from this sample has a finite width which scales with the absolute strength of the spurious gradients. When one applies the encoding gradient G_z to perform a one-dimensional MRI projection along the z -axis, the initial width of the NMR line determines the strength of the gradient which must be applied to distinguish the separate contributions to the NMR spectrum from the two spatially distinct regions of the phantom.

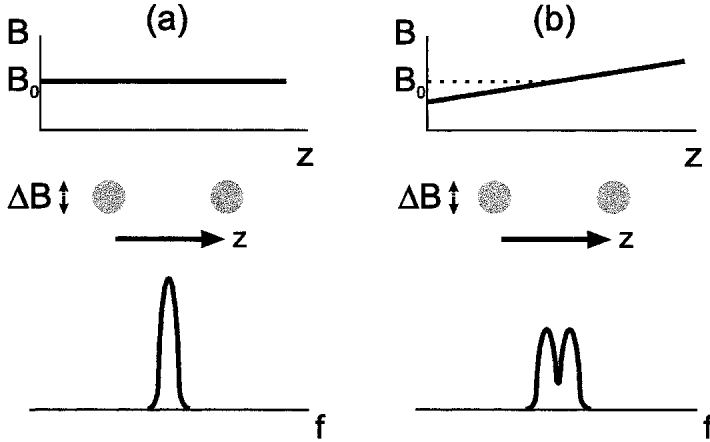


Fig. 8. Relationship between spectral and spatial resolutions. (a) NMR spectrum without an applied gradient showing inhomogeneous broadening of the line. (b) NMR spectrum with an applied gradient G_z that barely resolves the two spatially separated regions of the phantom. If the bare NMR line is narrow, only a small gradient needs to be applied.

We see that the spatial resolution Δz attainable in such an experiment is determined from the relation

$$\Delta z = 2\pi\Delta f/\gamma G_z, \quad (9)$$

where Δf is the width of the NMR line in the absence of an applied gradient.

We emphasize that the important quantity is the NMR linewidth, which is determined by the *absolute* homogeneity of B_0 . As was discussed in Sec. 3, absolute field homogeneity is automatically enhanced for a given coil configuration by reducing B_0 . In the case of NMR detection with an untuned SQUID magnetometer, the reduction in measurement field entails no signal loss provided that the sample magnetization is fixed, for example by pre-polarization in a strong transient field. The basis of SQUID-detected MRI in microtesla fields is then as follows. The sample of nuclear spins is pre-polarized in field of the order of 100 mT. However, instead of detecting the NMR signal in this field, where it is quite challenging to achieve a narrow NMR linewidth, one measures the NMR signal in an extremely low magnetic field, where it is possible to approach the lifetime limited linewidth even for grossly inhomogeneous measurement fields. Now it is necessary to apply only modest magnetic field gradients to perform the encoding. As a result, the NMR signal is dispersed over only a narrow band. The NMR transients are therefore detected with high SNR, and the time required to acquire the

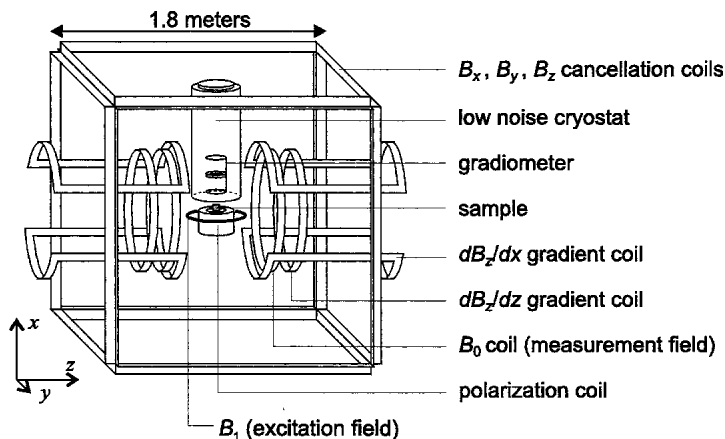


Fig. 9. Schematic of the low field SQUID MRI system showing magnetic field and gradient coils and a liquid helium dewar. For clarity, coils for encoding gradient G_y and slice selection gradient G_x are not shown.

image is relatively short.

Once the measurement field has been reduced below the strength at which its inhomogeneity distorts the image, the choice of field depends largely on environmental noise. We chose a 5.6 kHz measurement frequency because it lies above the 60 Hz power line harmonics in our laboratory and because noise at this frequency can be effectively shielded by a modest thickness of Al plate (Section 4.2.3). The corresponding measurement field of 132 μT is also high enough to avoid image artifacts caused by concomitant gradients (Section 4.4).

4.2. Experimental Configuration

To implement these ideas, we constructed the SQUID-based MRI system shown schematically in Fig. 9. The system incorporated three sets of coils used to cancel the Earth's field over the imaging region; a pair of coils used to provide a weak measurement field B_0 ; four sets of gradient coils, two used for image encoding, one for slice selection, and one for shimming; an excitation coil; a compact polarizing field coil; and a liquid helium dewar which housed the SQUID receiver. In the following subsections we describe each component of the system in detail, with special attention to the issue of noise.

4.2.1. SQUID probe and liquid helium cryostat

Because the sensitivity of the receiver sets the minimum noise floor for our MRI system, we first discuss the SQUID, which was based on Nb thin films and Nb-AlOx-Nb tunnel junctions. The input circuit consisted of a Nb-wire pickup coil wound as a 1+2+1 turn, second-order axial gradiometer with 150 mm baseline and 65 mm loop diameter, connected to a multiturn input coil integrated onto the SQUID chip. The effective sensing area of a single loop of the gradiometer was

$$A_{\text{eff}} = A_p M_i / (L_i + L_g) \approx 10 \text{ mm}^2 \quad (10)$$

where $L_i = 1.9 \mu\text{H}$ is the inductance of the input coil, $L_g = 1.7 \mu\text{H}$ is the estimated inductance of the gradiometer, $M_i = 11 \text{ nH}$ is the mutual inductance between the input coil and SQUID washer, and $A_p = 3.2 \cdot 10^{-3} \text{ m}^2$ is the geometric area of a pickup coil loop. The SQUID was operated in a flux-locked loop with flux modulation at 2 MHz. The measured flux noise in the flux locked loop was $7 \mu\Phi_0 \text{ Hz}^{-\frac{1}{2}}$, yielding a magnetic field noise of $1.5 \pm 0.2 \text{ fT Hz}^{-\frac{1}{2}}$ relative to a single loop of the gradiometer.

The sample to be imaged was placed directly under the tail of the cryostat. To maximize the filling factor, the sensing loop of the gradiometer was pressed against the inner vessel of the double-walled cryostat which was used to isolate the SQUID receiver thermally from the room-temperature sample. As a result, the SQUID was tightly coupled to metallic components in the insulation jacket of the cryostat which generate Nyquist noise currents and hence magnetic field noise. In the G-10 fiberglass cryostat originally used in our experiments, Nyquist currents in the aluminized mylar ("superinsulation") or in the copper mesh of the thermal shield gave rise to a magnetic field noise of roughly $10 \text{ fT Hz}^{-\frac{1}{2}}$ referred to the sensing loop of the second-order gradiometer, exceeding the intrinsic noise of the receiver by an order of magnitude.

To reduce the magnetic field noise contribution of the superinsulation substantially, we constructed a G-10 fiberglass dewar based on the design of Seton *et al.*²⁹ In this dewar, shown schematically in Fig. 10, the normal metal thermal shield was replaced by a shield consisting of an array of 180 1-mm-diameter alumina rods attached to a thin G-10 fiberglass shell with epoxy. The thermal shield was anchored to the top of the inner vessel of the dewar by 180 1-mm-diameter Al wires, and was capped at the bottom with a thin alumina disc. Since the thermal shield had a high thermal conductivity, it was efficiently cooled by the He gas which evaporated from the inner vessel. However, as the shield was electrically insulating, it did not give rise to magnetic field noise. To minimize magnetic field noise from the

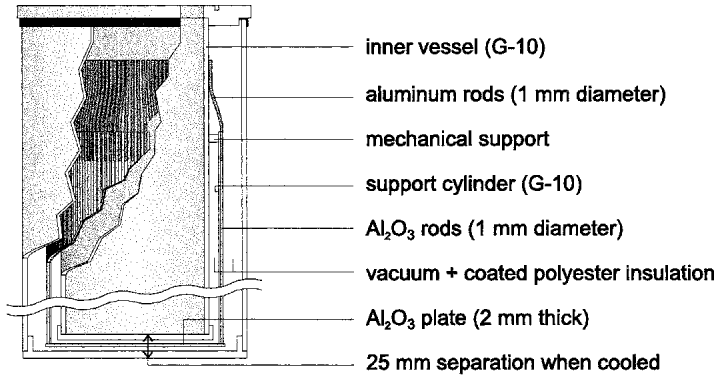


Fig. 10. Cutaway view of the low noise liquid helium dewar. The thermal shield that surrounds the inner vessel comprises alumina rods and disk attached on a thin fiberglass shell. The superinsulation in the vacuum space is made of aluminized polyester cloth to minimize the Nyquist noise from the metallization.

multilayer superinsulation, we replaced the conventional aluminized mylar with aluminized polyester fabric.²⁹ In this case, the weave of the fabric broke up continuous conducting paths to prevent the flow of noise currents over large areas. The magnetic field noise generated by the metallization therefore fell away rapidly with distance from the multilayer insulation.

The inner vessel of the cryostat was 0.82 m deep and its inner diameter of 102 mm could easily accommodate the large-area pickup coils needed for SQUID MRI. The separation from the liquid helium space to the room temperature outside surface was 25 mm. The capacity of the cryostat was approximately 6 L, and the hold time was 40 hours. The measured magnetic field noise of the cryostat was less than $1 \text{ fT Hz}^{-\frac{1}{2}}$.

4.2.2. Coils and electronics

The geometries and specifications of the magnetic field and gradient coils are summarized in Table 1. The Earth's field cancellation coils were wound on the six faces of a wooden cube approximately 2 m on a side. Wooden braces integrated into the cube supported a coil assembly which included the measurement field and gradient coils. The measurement field coils were wound as a Helmholtz pair, while the coils which produced the diagonal (G_z) and off-diagonal (G_x and G_y) gradients were wound in the Maxwell and Golay geometries, respectively.³⁰ The G_y and G_z coils provided

Function	Geometry	Turns, wire dia. Inductance Resistance	Typical field/ field gradient Current
Cancellation field B_x, B_y, B_z	Square coils on opposite sides of the 1.8 m cube	100, 1.0 mm 110 mH 30 Ω	25 μ T 0.5 A
Measurement field B_z	Helmholtz pair; radius 0.6 m	20, 1.0 mm 3.3 mH 3.7 Ω	132 μ T 4.4 A
Excitation field B_x	Circular coil; 230 mm diameter	15, 0.8 mm 93 μ H 0.8 Ω	33 μ T 0.3 A
Polarization field B_x	Solenoid; height 150 mm, I.D. 50 mm, O.D. 150 mm	800, 2.0 mm 32 mH 1.4 Ω	300 mT 40 A
Shimming gradient dB_z/dx	Golay coil; radius of curvature 0.6 m	20, 0.8 mm 0.53 mH 2.4 Ω	5 μ T/m 0.4 A
Encoding gradient dB_z/dy	Golay coil; radius of curvature 0.6 m	40, 0.8 mm 2.2 mH 3.8 Ω	100 μ T/m 4 A
Encoding gradient dB_z/dz	Maxwell pair; radius 0.6 m	20, 1.0 mm 3.1 mH 3.5 Ω	100 μ T/m 2 A
Slice selection gradient dB_z/dx	Biplanar coil; four 700 \times 380 mm rectangular loops	20, 1.0 mm 3.1 mH 4.8 Ω	400 μ T/m 2 A

Table 1. Magnetic field coils used in the microtesla MRI system

encoding gradients. We used the G_x coil to cancel a parasitic gradient by adjusting the current to minimize the NMR linewidth; the parasitic G_y and G_z components were negligible. A set of rectangular biplanar gradient coils (not shown in Fig. 9) was used to apply large- amplitude slice selection gradients in the x -direction. The wooden braces also supported the helium dewar containing the SQUID sensor. The polarizing coil was placed below the dewar. Samples were placed in the 10 mm gap between the polarizing coil and the dewar or in the 50 mm bore of the polarizing coil. The excitation coil was wound on a G- 10 fiberglass form which surrounded the polarizing coil; spin manipulation was performed using resonant audiofrequency pulses applied along the detection direction. We chose the dimensions of the system

with an eye to the eventual imaging of human subjects.

The Helmholtz pair that produced the 132 μT measurement field was driven by a current-controlled power supply at a current of 4.6 A. The gradient coils were driven by a Techron linear amplifier (LVC 2016) with a maximum output voltage of 30 V, resulting in a maximum current through the coils of about 8 A. To reduce the voltage needed to drive the Golay coils, the four components of each coil were wired in parallel. When connected to their respective amplifiers, neither the measurement field coil nor the gradient coils increased the system noise above the intrinsic noise of the SQUID receiver. Since the excitation coil was strongly coupled to the gradiometer, a mechanical relay was used to disconnect the coil from its power supply during data acquisition to prevent coupling of external noise to the SQUID. A mechanical relay was also used to open the G_x -Golay coils to prevent slice selection gradient pulses from inducing spurious currents into them.

The polarizing coil was driven with a voltage pulse from a Techron 7700 power amplifier. The voltage was ramped up to 100 V, held constant for a time long compared to T_1 , and then switched to -100 V in order to bring the current to zero rapidly. The heat generated by this 4 kW pulse was conducted away by 120 vertical sections of 1 mm diameter Cu wire inserted between windings of the solenoid. These wires were attached to a Cu tube underneath the solenoid; a continuous flow of liquid N₂ cooled the Cu tube. The polarizing coil was strongly coupled to the gradiometer and contributed a noise $\sim 20 \text{ fT Hz}^{-\frac{1}{2}}$ when connected to its amplifier. We greatly reduced this additional noise by opening mechanical relays in series with the polarizing coil after turning off the polarizing field. This procedure decoupled the SQUID gradiometer from noise generated by the amplifier and from external noise coupled in through the current leads of the polarizing coil. The remaining $3 \text{ fT Hz}^{-\frac{1}{2}}$ noise from the polarizing coil originated from Nyquist noise currents flowing across the 2 mm diameter Cu wire of the coil, and was the dominant noise source in the system.

We used a Tecmag Orion System with gradient control unit to produce the imaging pulse sequences and digitize the SQUID signal. This system generated voltage pulses to drive the polarization and excitation coils and controlled the voltages applied to the gradient coils for image encoding. The mechanical relays for opening the connections to the polarizing and excitation coils were switched with digital output lines. A Princeton Applied Research 113 preamplifier with a 1–10 kHz bandpass filter amplified the signal from the flux-locked loop. The Tecmag's 16-bit analog-to-digital converter digitized the preamplifier output; subsequent signal processing was performed in software.

4.2.3. *Environmental magnetic field noise*

The spectral density of the magnetic field fluctuations in our laboratory exhibits a rich structure. There are discrete peaks at 60 Hz and its harmonics. At frequencies of a few kilohertz, away from these harmonics, the magnetic field noise appears to be “quasi-white,” with an amplitude of $1 \text{ pT Hz}^{-\frac{1}{2}}$. Below 100 Hz, where magnetic field fluctuations are dominated by the movement of large magnetic objects, such as elevators and automobiles, and by low-frequency activity on the power grid, the magnetic field noise increases rapidly. When one designs a low-field SQUID MRI system, the options are to reject the noise from distant sources of interference by using a SQUID gradiometer, to adjust the measurement field to steer the imaging band into a clean part of the spectrum of environmental field fluctuations, or to implement passive (for example, eddy-current) shielding of the MRI system. We adopted a combination of all three approaches.

Our second-order gradiometer achieved an “as-made” balance of one part in a few hundred against uniform magnetic fields (applied either in-plane or out-of-plane). With this level of rejection, the environmental contribution to the system noise was reduced to around $10 \text{ fT Hz}^{-\frac{1}{2}}$. In principle, we might have improved the gradiometer balance by either analog electronic or software balancing schemes, involving subtraction from the gradiometer signal of suitably scaled (and perhaps phase-shifted) signals from reference SQUID magnetometers and first-derivative gradiometers. At 5.6 kHz, however, such schemes are difficult to implement, due, for example, to frequency-dependent phase shifts induced by eddy currents in nearby metallic objects such as structural steel in the building or metallic components in the dewar. Instead we chose passive shielding and constructed an eddy current shield from 3-mm-thick 5052 Al plate to surround the MRI system. At 5.6 kHz, 3 mm corresponds to about two skin depths so that the shield attenuated magnetic field fluctuations by an order of magnitude. This level of rejection effectively eliminated the environmental contribution to the noise of the system. Furthermore, we ensured that the eddy-current shield was rf-tight, thereby eliminating high-frequency interference which would otherwise suppress the flux-to-voltage transfer function of the SQUID and degrade its noise performance.

Aside from contributing to the SQUID noise, external magnetic field interference also affected spin precession in the sample. If we apply a small-amplitude oscillatory field $B_{\text{ext}} \cos \omega_{\text{ext}} t$ in addition to the measurement field B_0 , the accumulated phase of the nuclear spins varies with time as

$$\theta(t) = \gamma \int_0^t (B_0 + B_{\text{ext}} \cos \omega_{\text{ext}} t') dt' = \omega_0 t + (\gamma B_{\text{ext}} / \omega_{\text{ext}}) \sin \omega_{\text{ext}} t. \quad (11)$$

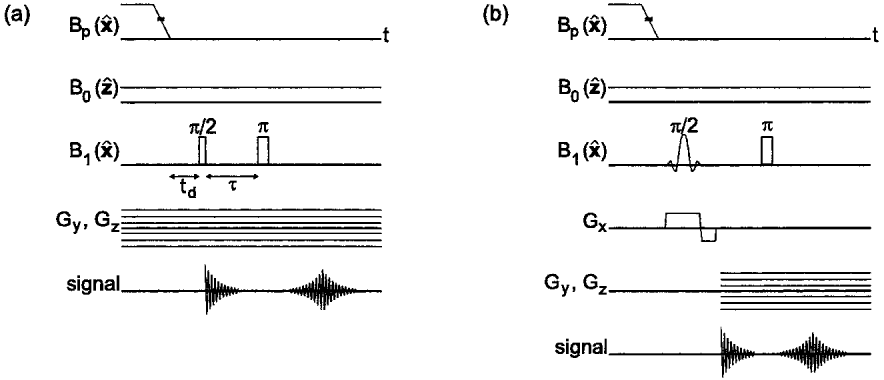


Fig. 11. Pulse sequences for microtesla field MRI. (a) Two-dimensional imaging with static magnetic field gradients. The direction of the gradient is stepped through successive values in the y - z plane; for each gradient direction, a one-dimensional projection is acquired. (b) Slice selected imaging.

The phase oscillates about its unperturbed value with angular frequency ω_{ext} and an amplitude that scales inversely with ω_{ext} . In the frequency domain, this perturbation produces sidebands at the frequencies $\omega_0 \pm n\omega_{\text{ext}}$. The 60 Hz peak-to-peak magnetic field is typically 50 nT in our laboratory. Using this value and taking the Fourier transform of Eq. (11), we find the $(\omega_0 \pm \omega_{\text{ext}})$ peaks are ~ 80 times weaker than the fundamental peak at ω_0 . Since a typical SNR for an image from our system is ~ 10 , the effect of power line harmonics on image quality is negligible. A much more serious issue, however, is the building elevator, which produces ~ 400 nT magnetic field variations at frequencies well below 1 Hz, corresponding to shifts in proton Larmor frequency of more than 15 Hz. These markedly degrade our images, requiring us to stop the elevator during imaging sessions.

4.3. Microtesla MRI: Sequences and Images

Although the pulse sequence of Fig. 5b provides a convenient way of performing broadband NMR at low fields without resonant spin manipulation, non-adiabatic switching of the polarization and measurement fields becomes increasingly difficult as the field strengths and the size of the coils are increased. For our MRI experiments conducted in measurement fields ~ 100 T, we adopted a pulse sequence involving adiabatic turnoff of the polarizing field and resonant spin manipulation (Fig. 11). All of the examples shown represent proton images.

4.3.1. Two-Dimensional Images

Figure 11a shows the sequence used to acquire two-dimensional images. The nuclear spins are prepolarized in a magnetic field $B_p \approx 300$ mT applied along the x -direction for a time which is long compared to T_1 . Upon adiabatic removal of the polarizing field, the sample magnetization reorients toward the much weaker measurement field $B_0 = 132 \mu\text{T}$, which is applied in a direction (z) orthogonal to the gradiometer pickup loop. Following a predetermined delay time t_d , a resonant $\pi/2$ pulse induces precession of the spins in the measurement and gradient fields; the spin echo signal formed by a resonant π pulse is detected by the SQUID sensor. The SQUID flux lock was enabled after the application of the π pulse; the time preceding the formation of the echo allowed ample time for the flux-locked loop to reset. As with the NMR experiments, a superconducting weak link prevented large currents from being coupled into the input coil of the SQUID during spin manipulation.

To demonstrate the principle of microtesla field MRI, we used the conceptually simple method of projection reconstruction⁵ to obtain two-dimensional images of phantoms and other samples. In this technique, the direction of the static magnetic field gradient was stepped through successive values to cover the half-circle (in the y - z plane); at each gradient direction, we acquired a one-dimensional MRI projection. The one-dimensional projections were then combined (using either filtered back projection³¹ or interpolation to a cartesian grid followed by a two-dimensional FFT) to obtain the full two-dimensional image.

Figure 12a shows the image acquired from an MRI phantom in a field of $132 \mu\text{T}$. Thirteen 40-mm-long columns were milled in a Teflon block and filled with mineral oil. The column diameters were 3.2 mm, 6.3 mm and 9.6 mm. The image was reconstructed from 48 one-dimensional projections acquired in a magnetic field gradient $G = 200 \mu\text{T/m}$. For each projection 16 spin echo signals were averaged together; the total acquisition time was 7.5 min. Even the smallest column is well resolved, indicating a resolution of about 1 mm.

Figure 13a shows the image of a bell pepper acquired at $132 \mu\text{T}$. To obtain the image, we cut a slice approximately 10 mm thick from the pepper and placed it under the dewar. The two-dimensional image was acquired using the pulse sequence of Fig. 11a. The image is a faithful reproduction of the photograph, with a resolution of ~ 1 mm.

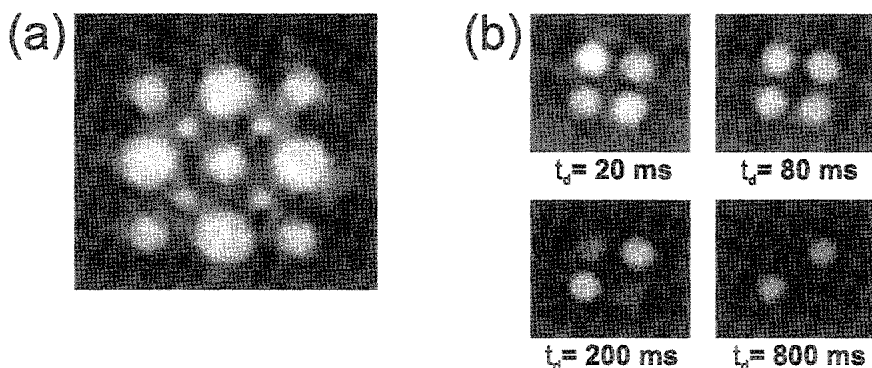


Fig. 12. Two-dimensional images of MRI phantoms at $132\ \mu\text{T}$. (a) Image of phantom consisting of 13 columns of mineral oil. Acquisition time 7.5 min. (b) T_1 -contrast images of four columns of water, with upper left and lower right columns doped with 1.0 mM Gd-DOTA. Four images with four values of t_d are shown.

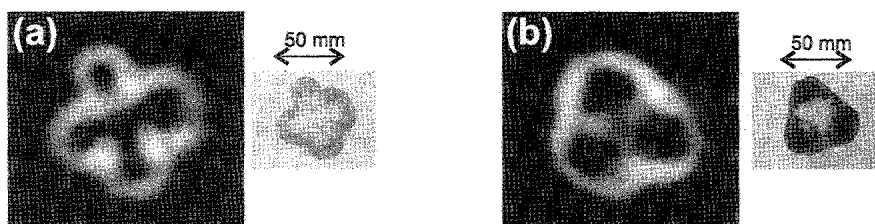


Fig. 13. MRI of bell peppers at $132\ \mu\text{T}$. (a) Two-dimensional image of bell pepper slice about 10 mm thick. Image was acquired with pulse sequence of Fig. 11a using 48 one-dimensional projections with $G = 100\ \mu\text{T/m}$. For each projection, 8 spin echo signals were averaged; total acquisition time was 5 min. Photograph of pepper slice is on the right. (b) Slice-selected image of whole pepper acquired with sequence of Fig. 11b. Slice thickness was 20 mm. Image was reconstructed from 24 one-dimensional projections with $G = 100\ \mu\text{T/m}$. For each projection, 4 spin echo signals were averaged; total acquisition time was 96 seconds. Photograph of the pepper slice, cut after the MRI, is on the right.

4.3.2. Slice Selection Imaging

In the MRI pulse sequence shown in Fig. 11a, the broadband $\pi/2$ pulse excites all the spins in the sample. The resulting MRI is therefore a projection of the three-dimensional object onto the y - z plane. To image a particular slice of the object, however, one can apply a narrowband $\pi/2$ pulse designed to excite only the spins in the selected slice. In the sequence of Fig. 11b, a narrowband $\pi/2$ pulse with a sinc $[(\sin x)/x]$ function envelope is applied in conjunction with a relatively strong gradient pulse $G_x \sim 400 \mu\text{T/m}$ in the direction normal to the plane of the slice. This excites only the spins in a slice of thickness $2\pi\delta f_1/\gamma G_x$, where $\delta f_1 \sim 300 \text{ Hz}$ is the bandwidth of the $\pi/2$ pulse. Following the excitation pulse, the gradient G_x is reversed to refocus the phase accumulated during slice selection. Subsequently the gradients G_y and G_z are switched on, and the remainder of the pulse sequence follows that of Fig. 11a.

Figure 13b shows an MRI slice of an intact pepper imaged with the slice selection sequence described above. Subsequently, the pepper was cut open through the imaging plane to enable us to take the photograph shown next to the MRI slice. We see that the slice-selected image is an excellent reproduction of the outer skin shown in the photograph, with an in-plane resolution $\sim 1 \text{ mm}$. However, the inner structure of the pepper is poorly imaged, reflecting the fact that the seeds contain a low density of mobile protons.

4.3.3. T_1 -Contrast Imaging

As previously mentioned, the sharp dependence of T_1 on correlation time at low frequencies is a strong motivation for imaging in low fields. Our experiment is easily adapted to probe T_1 in microtesla fields. To illustrate T_1 -contrast imaging, we prepared a phantom containing four columns of water, two of which were doped with 1.0 mM of the paramagnetic contrast agent Gd-DOTA (Dotarem[®], Guerbet, Roissy, France). We imaged the phantom four times using the pulse sequence of Fig. 11a, varying the delay time t_d between adiabatic removal of B_p and initiation of the $\pi/2$ pulse from 20 ms to 800 ms; for each image, we acquired 24 single-shot projections with a polarizing time of 1 s. The images are shown in Fig. 12b. For $t_d = 80 \text{ ms}$, the pure water and Gd-doped columns have comparable brightnesses. However, as t_d is increased, the intensity of the Gd-doped water diminishes much more rapidly than the pure water, indicating a much shorter T_1 . A further inspection of Fig. 12b reveals that at $t_d = 20 \text{ ms}$ the Gd-doped water has a higher intensity than pure water, reflecting the higher degree of

polarization of the former because of its shorter T_1 (estimated to be ~ 0.1 s).

4.4. Concomitant Gradients

As the measurement field B_0 is reduced to the point where it becomes comparable to the fields produced by the gradient coils, one encounters image artifacts due to unwanted concomitant gradient components. Because $\text{div } \mathbf{B} = \text{curl } \mathbf{B} = 0$ for the total field \mathbf{B} at any point, any magnetic field gradient along one direction must be accompanied by a gradient along another direction. For example, the G_y gradient produced by the Golay coils is accompanied by a dB_y/dz gradient of equal magnitude. The total field magnitude is thus

$$|\mathbf{B}(\mathbf{r})| = B_0 + yG_y + z^2G_y^2/2B_0 + O(G_y^3). \quad (12)$$

The third term increases the precession frequency of spins at large values of $|z|$, causing an apparent change in position $z^2G_y/2B_0$. Choosing G_y to obtain resolution Δy using Eq. (9), we require

$$B_0 > (\pi\Delta f/\gamma)(z/\Delta y)^2 \quad (13)$$

for the concomitant gradient distortion to be smaller than Δy . To image the 30 mm x 30 mm mineral oil phantom of Fig. 12a (NMR linewidth ~ 5 Hz) with 1 mm resolution requires a gradient of 120 $\mu\text{T/m}$ and a minimum measurement field of 13 μT , well below the applied 132 μT . While the issue of concomitant gradients can be neglected for the present field strengths and sample sizes, it may become important for larger samples. For example, a system designed to image the human brain (size ~ 0.2 m and NMR linewidth ~ 1 Hz) with 1 mm resolution would require a gradient of 23 $\mu\text{T/m}$ and a measurement field greater than 120 μT .

5. DISCUSSION

We have seen that by reducing the magnitude of the measurement field and prepolarizing the nuclei in a much higher magnetic field one can use SQUID detection to obtain NMR spectra with high spectral resolution and high SNR at frequencies of a few hundred hertz. As examples of this technique, we showed that resonance splittings due to J -coupling—unencumbered by chemical shift—could readily be detected, and that the spectra of different nuclear species could be measured simultaneously. This

technique could be extended to a more general study of chemical bonds involving J -coupling. Since each bond produces a unique splitting, one could also use this method to identify unknown substances. Thus, low-frequency, high-resolution NMR could detect specific substances in blood samples, perhaps following the addition of a suitable reagent to generate a characteristic J -coupling splitting. An extension of this idea is the use of a "spy nucleus" to investigate whether a reagent is taken up by a particular site in the body.³²

We extended the principles of low-field NMR to low-field MRI, and demonstrated two-dimensional imaging, slice-selected imaging and T_1 -contrast imaging. Although the acquisition times are long by the standards of high-field MRI, we believe they can be reduced substantially. The magnetic field noise of the system is currently about $3 \text{ fT Hz}^{-\frac{1}{2}}$, and is set by Nyquist noise currents which flow in the Cu wire of the polarizing coil. This source of noise could be greatly reduced by replacing the solid wire with a finely braided (litz) wire with the same cross section. Furthermore, using a SQUID with a lower flux noise could be expected to reduce the intrinsic magnetic field noise of the detector from the current $1.5 \text{ fT Hz}^{-\frac{1}{2}}$ by at least a factor of 3. Obviously, to take full advantage of the reduction in intrinsic noise, one would have to reduce the detected environmental noise by a similar factor. This could likely be achieved by improving the balance of the second-order gradiometer,³³ which currently rejects uniform magnetic field noise by one part in only a few hundred. An alternative approach might be to operate the system in a more heavily shielded room.³³ We note that, for a given SNR, the imaging time scales inversely as the square of the magnetic field noise. Multiple spin echoes⁵ following each polarization could further improve the SNR. Furthermore, to increase sensitivity to dipole sources, it would be advantageous to replace the single gradiometer with its 65-mm loops with an array of smaller-area gradiometers, each coupled to its own SQUID. For a pick-up loop of radius r , the signal flux coupled to the loop from a dipole scales approximately as r^{-1} , whereas the noise flux due to remote sources of interference scales as r^2 . Thus, the use of a modest number of SQUID sensors could further improve the spatial resolution and acquisition efficiency dramatically.

An additional improvement in the overall performance of the system would result from replacing our current back-projection technique of acquiring images with a more advanced imaging modality such as phase encoding.⁵

What are the potential clinical applications of SQUID-based, low-field MRI? While such a system will never compete with high-field MRI for resolution and versatility, nonetheless, there are a number of dedicated applications where it could be implemented. A system with the demonstrated spatial resolution and anticipated improved imaging speed could be used to

image peripheral parts of the body, for example, arm and leg joints.¹⁴ Another important application—given the potentially low cost of the system and demonstrated T_1 -contrast capability—might be screening for breast cancer. Perhaps the most immediate application, however, is the combination of low-field MRI with existing commercial systems used for magnetic source imaging (MSI) of the brain. In MSI, weak (~ 10 fT) neuromagnetic signals are measured by an array of up to 300 SQUIDS, coupled to gradiometers, at frequencies up to about 100 Hz. This technique is rapidly becoming more widespread in clinical use, particularly for locating epileptic foci and presurgical screening of brain tumors, and represents the largest commercial market for SQUID sensors. While sophisticated software algorithms enable one to localize magnetic sources from the data acquired by the array, in practice the MSI must be combined with an MRI to correlate the magnetic sources with anatomical structure. The ability to perform low-field MRI with the sensors of the MSI array would greatly increase the utility of MSI, creating a versatile, new tool for both fundamental studies and clinical diagnosis of the human brain.

ACKNOWLEDGEMENTS

This work was supported by the Director, Office of Science, Office of Basic Energy Sciences, Division of Materials Sciences and Engineering of the U.S. Department of Energy. B. ten Haken thanks the Technology Foundation STW, Applied Science Division of NWO and the Technology Programme of the Ministry of Economic Affairs for support, M. Mößle acknowledges the “Deutsche Forschungsgemeinschaft” for a postdoctoral fellowship, and A. H. Trabesinger acknowledges the Swiss National Science Foundation for a postdoctoral fellowship.

REFERENCES

1. A. Abragam, *The Principles of Nuclear Magnetism*, Oxford University Press, London, (1961).
2. C.P. Slichter, *Principles of Nuclear Magnetic Resonance*, 3rd ed., Springer Verlag, New York (1990).
3. P.C. Lauterbur, *Nature* **242**, 190 (1973).
4. P. Mansfield and P.K. Grannell, *J. Phys. C Solid State* **6**, L422 (1973).
5. P.T. Callaghan, *Principles of Nuclear Magnetic Resonance Microscopy*, Clarendon, Oxford (1991).
6. M. Packard and R. Varian, *Phys. Rev.* **93**, 941 (1954).
7. A. Macovski and S. Connolly, *Magn. Reson. Med.* **30**, 221 (1993).

8. J. Stepišnik, V. Eržen, and M. Kos, *Magn. Reson. Med.* **15**, 386 (1990).
9. G.J. Béné, *Phys. Rep.* **58**, 213 (1980).
10. J. Clarke, in *SQUID Sensors: Fundamentals, Fabrication and Applications*, H. Weinstock (ed.), Kluwer Academic Publishers, Dordrecht (1996).
11. Ya.S. Greenberg, *Rev. Mod. Phys.* **70**, 175 (1998).
12. R. McDermott, A.H. Trabesinger, M. Mück, E.L. Hahn, Alex Pines, and John Clarke, *Science* **295**, 2247 (2002).
13. R. McDermott, S-K. Lee, B. ten Haken, A.H. Trabesinger, Alex Pines, and John Clarke, unpublished.
14. H.C. Seton, J.M.S. Hutchison, and D.M. Bussell, *Meas. Sci. Technol.* **8**, 198 (1997).
15. R.C. Jaklevic, J. Lambe, A.H. Silver, and J.E. Mercereau, *Phys. Rev. Lett.* **12**, 159 (1964).
16. B.D. Josephson, *Phys. Lett.* **1**, 251 (1962).
17. F. London, *Superfluids*, Wiley, New York (1950).
18. W.C. Stewart, *Appl. Phys. Lett.* **12**, 277 (1968).
19. D.E. McCumber, *J. Appl. Phys.* **39**, 3113 (1968).
20. M.B. Ketchen and J.M. Jaycox, *Appl. Phys. Lett.* **40**, 736 (1982).
21. M. Gurvitch, M.A. Washington, and H.A. Huggins, *Appl. Phys. Lett.* **42**, 472 (1983).
22. C.D. Tesche and J. Clarke, *J. Low Temp. Phys.* **27**, 301 (1977).
23. E.L. Hahn, *Phys. Rev.* **80**, 580 (1950).
24. W.G. Proctor and F.C. Yu, *Phys. Rev.* **77**, 717 (1950).
25. E.L. Hahn and D.E. Maxwell, *Phys. Rev.* **88**, 1070 (1952).
26. C.H. Tseng, G.P. Wong, V.R. Pomeroy, R.W. Mair, D.P. Hinton, D. Hoffmann, R.E. Stoner, F.W. Hersman, D.G. Cory, R.L. Walsworth, *Phys. Rev. Lett.* **81**, 3785 (1998).
27. M. Goldman, *Quantum Description of High-Resolution NMR in Liquids*, Clarendon, Oxford (1988).
28. G. Planinšič, J. Stepišnik, and M. Kos, *J. Magn. Reson.* **A110**, 170 (1994).
29. H.C. Seton, D.M. Bussell, and J.M.S. Hutchison, *Liquified Gas Cryostat*, UK Patents GB2331798 and GB2351549.
30. P.A. Bottomley, *J. Phys. E Sci. Instrum.* **14**, 1081 (1981).
31. A.K. Jain, *Fundamentals of Digital Image Processing*, Prentice Hall, Englewood Cliffs (1989).
32. A.H. Trabesinger, R. McDermott, S-K. Lee, M. Mück, John Clarke, and Alex Pines, *J. Phys. Chem.*, to be published.
33. J. Vrba, in *SQUID Sensors: Fundamentals, Fabrication and Applications*, Kluwer Academic, Dordrecht (1996), pp. 117–178.